ICCFD13-2026-074

A Two-Fluid Space–Time Cut-Cell Method for Heat and Mass Transfer

L. Libat*, C. Selçuk*, E. Chénier* and V. Le Chenadec*
Corresponding author: louis.libat2@univ-eiffel.fr
* MSME, Université Gustave Eiffel, UMR CNRS 8208, Marne-la-Vallée, 77454, France

Abstract:
This work presents a two-fluid, space–time cut-cell finite-volume method for conservative convective-diffusive transport of heat and mass across sharp and moving interfaces. The method maintains separate phase-side unknowns in cut cells and imposes interface conditions as algebraic constraints with interfacial unknowns. This dual-unknown approach naturally accommodates Henry partition laws, Kapitza thermal resistance and more complex phase change laws. It does not resort to one-fluid effective properties or reconstruction techniques within mixed cells. The finite-volume discretization is built on moment-based cut-cell geometry and inherits conservative flux balances at the discrete level. For moving interfaces, space–time integration combines the physical convective transport with the geometric sweeping flux through the relative velocity. The method is validated on benchmarks of increasing complexity: static Henry jump on a circular disk, co-moving convective Henry transport, and a spherical Kapitza thermal resistance case with co-moving interface. Numerical results show robust convergence, with near-second-order behavior in the bulk and robust resolution of interfacial jumps and flux residuals across multiple physical regimes.

Keywords: heat and mass transfer, cut-cell method, conservative convection, space–time discretization, Henry law, Kapitza resistance, sharp-interface method, two-fluid method, geometric conservation law.

1. Introduction

Sharp-interface heat and mass transfer across immiscible phases is governed by local conservation laws together with interfacial (thermodynamic) closure. In mass transfer, the concentration traces on the two sides of the interface are often related by a partition or Henry law, while the flux must satisfy a conservative balance. This combination is numerically demanding because the fluxes and the unknowns may be discontinuous across the interface [1, 2, 3]. In moving configurations, the difficulty increases further because the interface moves relative to the flow.

Body-fitted and arbitrary Lagrangian–Eulerian formulations represent the interface explicitly and therefore offer a natural way to impose flux and jump conditions on a material surface [4]. Their main limitation is practical rather than conceptual: complex geometries and moving interfaces require mesh generation, mesh motion, or remeshing, and conservative time integration must respect a geometric conservation law (GCL) to avoid spurious sources induced by grid motion [5]. Interface-capturing methods such as volume-of-fluid and level-set methods avoid remeshing and handle large deformation or topology changes on fixed grids [6, 7, 8]. However, in a standard classical one-fluid formulation, a cut or mixed cell contains effective material properties and a single scalar representation that cannot accommodate the multiple values that describe the original problem. That strategy is robust for many flows, but it is not naturally adapted to sharp Henry jumps or to separate phase-side concentrations unless additional reconstruction and interfacial closure machinery is introduced [9].

Recently, within the interfacial mass-transfer community, several such techniques have been developed within VOF or hybrid VOF/immersed-boundary frameworks. Reactive and non-reactive gas–liquid

transfer has been modeled with VOF methods by imposing Henry equilibrium and by reconstructing local interfacial fluxes [10, 11]. Continuous-species-transfer (CST) and single-field VOF formulations further improve robustness for large solubility and diffusivity contrasts, including local volume changes and non-isothermal extensions [12, 13]. Recent VOF-CST variants also target pore-scale CO_2 dissolution, oil swelling, and carbon storage applications by adding symmetric transfer terms to control the effective interface displacement [14]. Hybrid VOF/immersed boundary DNS has also been used for mass transfer and mixing in complex vessels, where the interface is handled by an immersed-boundary method [15]. These works show the maturity of interface-capturing approaches for practical gas–liquid mass transfer, but they still rely on reconstructed or volume-averaged interface states inside mixed cells. The present work instead keeps two separate phase unknowns and imposes the interfacial partition and flux balance directly as cut-cell finite-volume equations.

Immersed-boundary and immersed-interface methods provide another fixed-grid route by embedding the interface into a Cartesian discretization and modifying the equations, forcing terms, or stencils near the boundary [16, 17, 18]. These methods are flexible and have been used successfully in many flow and diffusion problems. For the present objective, the central issue is that heat or species transfer rates are finite-volume fluxes through a sharp interface. A method that does not explicitly keep the two phase-side balances and the interfacial exchange in conservative form imposes additional treatment to guarantee exact local cancellation of the fluxes and a proper enforcement of the partition law.

Embedded-boundary and cut-cell finite-volume methods address this conservation requirement more directly. The control volumes are the mathematical intersections of the Cartesian cells with the physical phases, and the integral balance is written on those phase-restricted volumes. This philosophy underlies Cartesian embedded boundary solvers for Poisson and heat equations [19, 20, 21, 22] and conservative Cartesian finite-volume methods for convection–diffusion in irregular domains [23]. The difficulty is shifted to the geometry: near the interface, the method needs volumes, apertures, centroids, and interface measures. Explicit construction of all cut polytopes can become cumbersome, especially in space–time, which motivates moment-based descriptions and quadrature tools for implicitly defined domains [24, 25, 26]. Recent cut-cell scalar-transport work further emphasizes that moving-interface calculations must integrate cut surfaces consistently in time in order to satisfy the geometric conservation law [27].

The method developed here follows this cut-cell finite-volume route but keeps a two-fluid representation. Each phase has its own cell-average unknowns, and cut cells also carry phase-side interfacial unknowns. This differs from one-fluid approaches in which the interface law must be folded into a lumped scalar or an effective coefficient in mixed cells. Very recent two-field work on structured meshes has shown the accuracy gains of phase reconstructions and two-phase cut-cell mass-flux approximations for static and moving diffusion tests, as well as for rising-bubble transfer, when compared with a classical one-fluid model [9, 28]. The present formulation instead solves the two phase equations simultaneously and imposes the interface flux balance and Henry jump as algebraic equations on the embedded interface unknowns. This structure was used previously for sharp-interface diffusion [29]; the originality of the present paper is to extend [29] to conservative convective–diffusive transport.

The key point is the treatment of convection at the embedded interface. On a fixed interface, the convective contribution must be included not only through ordinary Cartesian faces but also through the interface part of each mixed cell. On a moving interface, Reynolds' theorem shows that this interfacial transport must be measured with the relative velocity $\mathbf{u} - \mathbf{w}$, where $\mathbf{u}$ is the phase velocity and $\mathbf{w}$ is the interface velocity. The space–time cut-cell balance therefore combines the physical convective flux with the geometric sweeping flux, while the geometric conservation law accounts for the change of phase volume between two time levels. A decisive consequence is that the Henry interface condition is transported consistently by the flow.

This paper is organized as follows. Section 2 presents the continuum model for two-phase convective–diffusive transport with interfacial jump and flux balance. Section 3 introduces the cut-cell geometry and the phase-side and interfacial unknowns. Section 4 describes the finite-volume discretization of the

bulk equations and the interface conditions, including the space–time treatment of convection. Section 5 presents numerical results for static and moving interface benchmarks. Finally, Section 6 summarizes the findings and discusses future work.

2. Continuum model

We consider a fixed computational domain $\Omega \subset \mathbb{R}^d$ occupied by two phases $\Omega^-(t)$ and $\Omega^+(t)$ separated by a sharp interface $\Gamma(t)$,

$$\Omega = \Omega^-(t) \cup \Gamma(t) \cup \Omega^+(t), \qquad \Omega^-(t) \cap \Omega^+(t) = \emptyset. \tag{1}$$

The unit normal $\mathbf{n}$ is oriented from $\Omega^-(t)$ to $\Omega^+(t)$, so that $\mathbf{n} \equiv \mathbf{n}^-$. The interface velocity is $\mathbf{w}$, with normal component $w = \mathbf{w} \cdot \mathbf{n}$. We refer to interfacial traces of a, namely the one-sided limiting values of $a^\pm$ on $\Gamma(t)$. For any quantity a admitting traces on both sides of $\Gamma(t)$, we define

$$[\![a]\!] = a^+ - a^-. \tag{2}$$

The primary transported quantity is the concentration $c^\pm$, as in standard two-phase mass-transfer models [1, 2]. In contrast with a purely normalized formulation, we keep the density $\rho^\pm$ in the conservative variable. Hence $\rho^\pm c^\pm$ is the conserved concentration density.

2.1 Bulk concentration transport

In each phase, the concentration satisfies the conservative convective–diffusive equation

$$\frac{\partial(\rho^\pm c^\pm)}{\partial t} + \nabla \cdot \left(\rho^\pm c^\pm \mathbf{u}^\pm + \mathbf{j}_c^\pm\right) = r_c^\pm \qquad \text{in } \Omega^\pm(t), \tag{3}$$

where $\mathbf{u}^\pm$ is the barycentric velocity, $r_c^\pm$ is a volumetric source term, and the diffusive flux is

$$\mathbf{j}_c^\pm = -\rho^\pm D^\pm \nabla c^\pm. \tag{4}$$

The finite-volume discretization is derived from the conservative form (3).

2.2 Interface balance and phase change

At a moving interface, the convective transport must be measured relative to the interface velocity, through the relative normal velocity $(\mathbf{u}^\pm - \mathbf{w}) \cdot \mathbf{n}$. When phase change occurs, the normal mass flux through $\Gamma(t)$ is denoted by $\dot{m}$ and defined by

$$\dot{m} = \rho^- \left(\mathbf{u}^- - \mathbf{w}\right) \cdot \mathbf{n} = \rho^+ \left(\mathbf{u}^+ - \mathbf{w}\right) \cdot \mathbf{n}. \tag{5}$$

Positive $\dot{m}$ corresponds to mass transfer from $\Omega^-(t)$ to $\Omega^+(t)$. In particular, in the pure-diffusion limit $\mathbf{u}^\pm = \mathbf{0}$, equation (5) gives $\dot{m} = -\rho w$ with $w = \mathbf{w} \cdot \mathbf{n}$, so positive $\dot{m}$ corresponds to $w < 0$, i.e. the interface is receding from Ω^+ into Ω^- and is consistent with mass entering Ω^+.

The general concentration balance at a phase-change interface is

$$\dot{m}[\![c]\!] + [\![\mathbf{j}_c \cdot \mathbf{n}]\!] = 0 \qquad \text{on } \Gamma(t). \tag{6}$$

Substituting the definition of $\dot{m}$ (5), this is equivalently written as the jump of the total (diffusive plus relative convective) normal flux,

$$[\![\mathbf{j}_c \cdot \mathbf{n} + \rho c \left(\mathbf{u} - \mathbf{w}\right) \cdot \mathbf{n}]\!] = 0 \qquad \text{on } \Gamma(t), \tag{7}$$

a form that will be directly discretized in the cut-cell framework (Section 3).

The flux balance (6) constrains the *jump* of concentrations but leaves the individual traces undetermined. They are closed by a partition relation. We write

$$[\![c]\!]^{\lambda} = c^{+} - \lambda c^{-}, \tag{8}$$

and impose

$$c^{+} - \lambda c^{-} = g_{\Gamma} \qquad \text{on } \Gamma(t), \tag{9}$$

where λ is a Henry or partition coefficient [2, 3]. When the source term $g_{\Gamma} = 0$, the homogeneous relation $c^{+} = \lambda c^{-}$ holds, which is the classical Henry equilibrium at the interface.

Several useful limits follow directly from (6) and (9). Without phase change ($\dot{m} = 0$), the Stefan condition reduces to continuity of the diffusive flux,

$$[\![\mathbf{j}_c \cdot \mathbf{n}]\!] = 0, \tag{10}$$

and together with (9) this gives the standard Henry-law transfer problem. When phase change is present but the bulk velocity vanishes ($\mathbf{u}^{\pm} = \mathbf{0}$), equations (5) and (6) with equal densities give $\dot{m} = -\rho w$ and the Stefan condition becomes

$$\rho w [\![c]\!] = [\![\mathbf{j}_c \cdot \mathbf{n}]\!], \tag{11}$$

which is the classical Stefan condition relating interface speed to the diffusive flux imbalance. When the interface is advected by the flow ($\mathbf{u}^{\pm} \cdot \mathbf{n} = \mathbf{w} \cdot \mathbf{n}$), the relative normal velocity $(\mathbf{u}^{\pm} - \mathbf{w}) \cdot \mathbf{n}$ vanishes on both sides and the balance (7) reduces to (10). These limiting cases are all recovered without modification of the discrete operators.

2.3 Thermal transport

The same formulation is used for temperature. In each phase,

$$\frac{\partial(\rho^{\pm} C_p^{\pm} T^{\pm})}{\partial t} + \nabla \cdot \left(\rho^{\pm} C_p^{\pm} T^{\pm} \mathbf{u}^{\pm} + \mathbf{q}_T^{\pm} \right) = r_T^{\pm}, \qquad \text{in } \Omega^{\pm}(t), \tag{12}$$

with

$$\mathbf{q}_T^{\pm} = -k^{\pm} \nabla T^{\pm}. \tag{13}$$

At a phase-change interface, the Stefan energy balance is

$$\dot{m} L + [\![\mathbf{q}_T \cdot \mathbf{n}]\!] = 0 \qquad \text{on } \Gamma(t), \tag{14}$$

where L is the latent heat.

The interface temperature is often assumed to be the equilibrium melting temperature T_m,

$$T = T_m \qquad \text{on } \Gamma(t). \tag{15}$$

The coupled heat–mass phase-change problem is then closed by equations (9), (6), (14), and (15).

2.4 Kapitza thermal resistance

The temperature continuity assumed in (15) breaks down when the interface itself presents a finite resistance to heat flow. The Kapitza resistance [30] (or thermal contact resistance) generalizes the interfacial temperature condition by allowing a temperature jump proportional to the normal heat flux. This boundary-layer phenomenon is particularly relevant for liquid–solid and vapor–liquid interfaces at scales where the continuum assumption is stretched, and for composite materials where the microscale texture introduces an effective resistance.

In the absence of phase change, the normal heat flux is still continuous across $\Gamma(t)$, but instead of enforcing an equilibrium temperature as in (15), one imposes

$$[\![\mathbf{q}_T \cdot \mathbf{n}]\!] = 0, \qquad \mathbf{q}_T \cdot \mathbf{n} = -\frac{[\![T]\!]}{R_K} \qquad \text{on } \Gamma(t), \tag{16}$$

where R_K is the Kapitza resistance (dimension: $\mathrm{K\,m^2/W}$). This condition is structurally analogous to the Henry partition law (9) for concentration: both relate a jump across $\Gamma(t)$ to the normal flux, and both reduce to standard continuity in the limit $R_K \to 0$ (or $\lambda = 1$, $g_\Gamma = 0$). This parallel structure is exploited in the unified discretization of Section 3. For composite materials and multiphase systems, condition (16) captures interfacial thermal effects without resolving the submicron boundary layer [31].

In summary, the continuum model is posed on the two-phase domain decomposition (1) with the jump operator (2). Bulk concentration transport (Section 2.1) couples the conservative balance with the diffusive flux (4); the interface balance and phase change (Section 2.2) introduce the weighted jump (8) and the pure-diffusion Stefan form (11); thermal transport (Section 2.3) mirrors this structure through (12) and (13); and the Kapitza resistance (Section 2.4) closes the interface temperature condition.

3. Cut-cell geometry and unknowns

The discretization relies on the moment-based Cartesian cut-cell geometry introduced in [29]. We recall only the definitions needed to introduce the concentration unknowns and the conservative convective–diffusive operators. The construction is presented in two space dimensions for clarity, but extends directly to three dimensions. The generic scalar Φ, storage coefficient C, and diffusivity K of [29] specialize here to the concentration c, the density ρ (or ρC_p for temperature), and ρD (or k for temperature), so that the reused operators are unambiguous.

Let $\{x_i\}_{i=0}^{N_x}$ and $\{y_j\}_{j=0}^{N_y}$ be the Cartesian grid lines in the x and y directions, respectively. Let Δ_i^1 and Δ_j^2 be the open intervals in x and y directions defined by:

$$\Delta_i^1 = \left]x_{i-\frac{1}{2}}, x_{i+\frac{1}{2}}\right[, \qquad \Delta_j^2 = \left]y_{j-\frac{1}{2}}, y_{j+\frac{1}{2}}\right[. \tag{17}$$

The Cartesian cells are defined by:

$$\Omega_{i,j} = \Delta_i^1 \times \Delta_j^2. \tag{18}$$

At time t, each Cartesian cell is decomposed into two phase-restricted cells

$$\Omega_{i,j}^{\pm}(t) = \Omega_{i,j} \cap \Omega^{\pm}(t), \tag{19}$$

and an interfacial fragment

$$\Gamma_{i,j}(t) = \Omega_{i,j} \cap \Gamma(t). \tag{20}$$

Thus,

$$\Omega_{i,j} = \Omega_{i,j}^{-}(t) \cup \Gamma_{i,j}(t) \cup \Omega_{i,j}^{+}(t), \tag{21}$$

with disjoint subsets. A cell is called mixed if $\Gamma_{i,j}(t) \neq \emptyset$.

The phase volumes are

$$V_{i,j}^{\pm}(t) = \int_{\Omega_{i,j}^{\pm}(t)} d\mathbf{x}. \tag{22}$$

Their centroids are denoted by

$$\mathbf{x}_{i,j}^{\pm}(t) = \frac{\displaystyle\int_{\Omega_{i,j}^{\pm}(t)} \mathbf{x}\, d\mathbf{x}}{V_{i,j}^{\pm}(t)}, \qquad V_{i,j}^{\pm}(t) > 0. \tag{23}$$

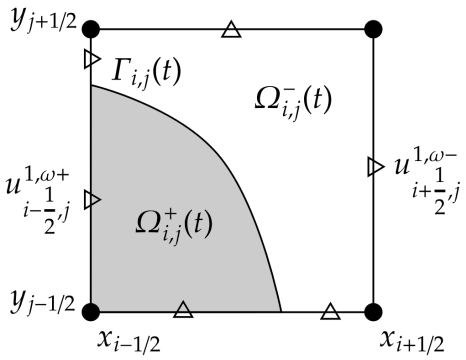

Figure 1: Cut-cell geometry and unknowns. The Cartesian cell $\Omega_{i,j}$ is decomposed into two phase-restricted cells $\Omega^-_{i,j}$ and $\Omega^+_{i,j}$, and an interfacial fragment $\Gamma_{i,j}$. The concentration unknowns are defined as phase averages over the phase-restricted cells (bulk unknowns) and as interface averages over the interfacial fragment (interface unknowns). The velocity components are defined as aperture averages on the staggered faces, and as an average on the interfacial fragment for the interface contribution of the convective flux.

If a phase is absent from a cell, the centroid is set to the Cartesian cell center. This convention allows the same algebraic definitions to be used in pure and cut cells.

The portions of Cartesian faces occupied by each phase are denoted by

$$\Sigma^{1\pm}_{i-\frac{1}{2},j}(t) = \left(\{x_{i-\frac{1}{2}}\} \times \Delta^2_j\right) \cap \Omega^{\pm}(t), \tag{24}$$

and

$$\Sigma^{2\pm}_{i,j-\frac{1}{2}}(t) = \left(\Delta^1_i \times \{y_{j-\frac{1}{2}}\}\right) \cap \Omega^{\pm}(t). \tag{25}$$

The corresponding face apertures are

$$A^{1\pm}_{i-\frac{1}{2},j}(t) = \int_{\Sigma^{1\pm}_{i-\frac{1}{2},j}(t)} dS, \qquad A^{2\pm}_{i,j-\frac{1}{2}}(t) = \int_{\Sigma^{2\pm}_{i,j-\frac{1}{2}}(t)} dS. \tag{26}$$

In addition to the volumes and face apertures, the cut-cell operators use the secondary moments

$$B^{1\pm}_{i,j}(t), \qquad B^{2\pm}_{i,j}(t), \qquad W^{1\pm}_{i-\frac{1}{2},j}(t), \qquad W^{2\pm}_{i,j-\frac{1}{2}}(t). \tag{27}$$

The quantities $B^{\alpha\pm}$ are phase apertures evaluated at the phase centroids, while $W^{\alpha\pm}$ are phase volumes between neighboring phase centroids across Cartesian faces. Their precise definitions are those of the moment-based cut-cell construction in [29]. They provide the geometric weights required to approximate fluxes and gradients without explicitly reconstructing the cut polyhedra.

The concentration unknowns are defined as phase averages over the phase-restricted cells. For every active phase volume,

$$c^{\omega\pm}_{i,j}(t) = \frac{\displaystyle\int_{\Omega^{\pm}_{i,j}(t)} c^{\pm}(t,\mathbf{x})\, d\mathbf{x}}{V^{\pm}_{i,j}(t)}, \qquad V^{\pm}_{i,j}(t) > 0. \tag{28}$$

The superscript ω denotes a bulk unknown. In time-discrete form,

$$c^{\omega\pm}_{n,i,j} = c^{\omega\pm}_{i,j}(t_n). \tag{29}$$

In each mixed cell, the two traces of the concentration on the interface are represented by interfacial unknowns,

$$c_{i,j}^{\gamma\pm}(t) = \frac{\displaystyle\int_{\Gamma_{i,j}(t)} c^{\pm}(t,\mathbf{x})\, dS}{\displaystyle\int_{\Gamma_{i,j}(t)} 1\, dS}, \qquad \Gamma_{i,j}(t) \neq \emptyset. \tag{30}$$

Their time-discrete counterparts are

$$c_{n,i,j}^{\gamma\pm} = c_{i,j}^{\gamma\pm}(t_n). \tag{31}$$

The two interfacial unknowns are used to impose the interface balance and the Henry or partition condition.

For convective transport, velocity components are located on staggered Cartesian faces. The phase-restricted face velocity in direction α is interpreted as an aperture average of the normal velocity,

$$u_{i-\frac{1}{2},j}^{1\omega\pm}(t) = \frac{\displaystyle\int_{\Sigma_{i-\frac{1}{2},j}^{1\pm}(t)} \mathbf{u}^{\pm}(t,\mathbf{x}) \cdot \mathbf{e}_1\, dS}{A_{i-\frac{1}{2},j}^{1\pm}(t)}, \tag{32}$$

and

$$u_{i,j-\frac{1}{2}}^{2\omega\pm}(t) = \frac{\displaystyle\int_{\Sigma_{i,j-\frac{1}{2}}^{2\pm}(t)} \mathbf{u}^{\pm}(t,\mathbf{x}) \cdot \mathbf{e}_2\, dS}{A_{i,j-\frac{1}{2}}^{2\pm}(t)}. \tag{33}$$

These velocities are the geometric inputs used to assemble the conservative convective fluxes through the cut faces. On a mixed cell, the velocity also has to be sampled on the embedded part of the boundary. We denote by $u^{\gamma\pm}$ the velocity used in the cut/interface contribution of the finite-volume divergence. In practice it is obtained with the same quadrature used for the interface moments, for instance

$$u_{i,j}^{\alpha\gamma\pm}(t) = \frac{\displaystyle\int_{\Gamma_{i,j}(t)} \mathbf{u}^{\pm}(t,\mathbf{x}) \cdot \mathbf{e}_\alpha\, dS}{\displaystyle\int_{\Gamma_{i,j}(t)} 1\, dS}, \qquad \alpha = 1,2. \tag{34}$$

The discrete formulas below use the oriented coefficients induced by the cut-cell divergence, so the sign of the interface normal is already contained in the corresponding geometric weights. The orientation of the interface contribution is carried by the geometric coefficients $B^{\alpha\pm} - A^{\alpha\pm}$; therefore $u^{\alpha\gamma\pm}$ denotes a Cartesian component, not a signed normal velocity. Figure 1 summarizes the geometric moments and the location of the bulk, interface, and staggered velocity unknowns.

For moving interfaces, the same definitions are lifted to the space–time slab $[t_n, t_{n+1}]$. The phase-restricted space–time control volume is denoted by

$$\left\{(t,\mathbf{x}) \;:\; t \in [t_n, t_{n+1}],\ \mathbf{x} \in \Omega_{i,j}^{\pm}(t)\right\}. \tag{35}$$

The corresponding space–time moments are written

$$\mathcal{V}^{\pm}, \qquad \mathcal{A}^{\alpha\pm}, \qquad \mathcal{B}^{\alpha\pm}, \qquad \mathcal{W}^{\alpha\pm}. \tag{36}$$

which are the space–time analogues of $V^{\pm}$, $A^{\alpha\pm}$, $B^{\alpha\pm}$, and $W^{\alpha\pm}$. In the moving case, these moments account for swept volumes, moving apertures, and fresh/dead-cell events.

4. Discrete operators

We now introduce the discrete operators used to approximate the conservative convective–diffusive concentration equation (3). The construction follows the moment-based cut-cell operators of [29], with the additional conservative convection operator written explicitly in terms of the bulk and interfacial concentration unknowns. For the sake of simplicity, we consider $\rho^{\pm}$, $D^{\pm}$ constant in each phase.

4.1 Fixed-interface operators

For a fixed interface, integrating the conservative equation (3) over a phase-restricted cell gives

$$\rho^{\pm}\frac{d}{dt}\left(V_{i,j}^{\pm}c_{i,j}^{\omega\pm}\right)+\int_{\partial\Omega_{i,j}^{\pm}\setminus\Gamma_{i,j}}\left(\rho^{\pm}c^{\pm}\mathbf{u}^{\pm}+\mathbf{j}_c^{\pm}\right)\cdot\mathbf{n}^{\pm}\,dS + \int_{\Gamma_{i,j}}\left(\rho^{\pm}c^{\pm}\mathbf{u}^{\pm}+\mathbf{j}_c^{\pm}\right)\cdot\mathbf{n}^{\pm}\,dS=\int_{\Omega_{i,j}^{\pm}} r_c^{\pm}\,dV. \quad (37)$$

The first term corresponds to the time derivative of the phase mass in the cell. The first surface integral is the exchange through phase-restricted Cartesian faces. The second surface integral corresponds to the embedded-interface contribution. The right-hand side is the volumetric source term.

4.1.1 Diffusive fluxes

The diffusive concentration flux is $\mathbf{j}_c^{\pm}=-\rho^{\pm}D^{\pm}\nabla c^{\pm}$. We factor out the density and work with the reduced flux

$$\mathbf{q}_c^{\pm}=-D^{\pm}\nabla c^{\pm},\qquad \mathbf{j}_c^{\pm}=\rho^{\pm}\mathbf{q}_c^{\pm}. \quad (38)$$

Restricting the diffusive part of the integral balance (37) to $\mathbf{q}_c^{\pm}$ alone, the Gauss theorem splits the boundary integral into a Cartesian-face contribution and an embedded-interface contribution,

$$\int_{\partial\Omega_{i,j}^{\pm}}\mathbf{q}_c^{\pm}\cdot\mathbf{n}^{\pm}\,dS=\underbrace{\int_{\partial\Omega_{i,j}^{\pm}\setminus\Gamma_{i,j}}\mathbf{q}_c^{\pm}\cdot\mathbf{n}^{\pm}\,dS}_{\text{Cartesian faces}}+\underbrace{\int_{\Gamma_{i,j}}\mathbf{q}_c^{\pm}\cdot\mathbf{n}^{\pm}\,dS}_{\text{embedded interface}}. \quad (39)$$

On mesh-aligned faces the outward normals are $\pm\mathbf{e}^{\alpha}$, so the Cartesian-face term takes the conservative flux-difference form

$$\int_{\partial\Omega_{i,j}^{\pm}\setminus\Gamma_{i,j}}\mathbf{q}_c^{\pm}\cdot\mathbf{n}^{\pm}\,dS=A_{i+\frac12,j}^{1\pm}Q_{i+\frac12,j}^{1\pm}-A_{i-\frac12,j}^{1\pm}Q_{i-\frac12,j}^{1\pm}+A_{i,j+\frac12}^{2\pm}Q_{i,j+\frac12}^{2\pm}-A_{i,j-\frac12}^{2\pm}Q_{i,j-\frac12}^{2\pm}, \quad (40)$$

where $Q^{\alpha\pm}$ denotes the normal diffusive flux averaged over the phase-restricted face. We define the directional volume-integrated divergence operators

$$\begin{cases}V_{i,j}^{\pm}\,\mathrm{div}_{i,j}^{1\omega}(A,Q):=A_{i+\frac12,j}Q_{i+\frac12,j}-A_{i-\frac12,j}Q_{i-\frac12,j},\\ V_{i,j}^{\pm}\,\mathrm{div}_{i,j}^{2\omega}(A,Q):=A_{i,j+\frac12}Q_{i,j+\frac12}-A_{i,j-\frac12}Q_{i,j-\frac12}.\end{cases} \quad (41)$$

The embedded-interface integral is approximated using the available reduced geometric moments. The approximation is designed to satisfy exact cancellation when the face fluxes are constant and to recover the classical divergence in pure cells. This yields

$$\int_{\Gamma_{i,j}}\mathbf{q}_c^{\pm}\cdot\mathbf{n}^{\pm}\,dS\simeq\left(B_{i,j}^{1\pm}-A_{i+\frac12,j}^{1\pm}\right)Q_{i+\frac12,j}^{1\pm}+\left(A_{i-\frac12,j}^{1\pm}-B_{i,j}^{1\pm}\right)Q_{i-\frac12,j}^{1\pm}+\left(B_{i,j}^{2\pm}-A_{i,j+\frac12}^{2\pm}\right)Q_{i,j+\frac12}^{2\pm}+\left(A_{i,j-\frac12}^{2\pm}-B_{i,j}^{2\pm}\right)Q_{i,j-\frac12}^{2\pm}, \quad (42)$$

formalized as the cut/interface divergence operators

$$\begin{cases} V^{\pm}_{i,j}\,\mathrm{div}^{1\gamma}_{i,j}(A,B,Q) := \left(B_{i,j} - A_{i+\frac{1}{2},j}\right) Q_{i+\frac{1}{2},j} + \left(A_{i-\frac{1}{2},j} - B_{i,j}\right) Q_{i-\frac{1}{2},j}, \\ V^{\pm}_{i,j}\,\mathrm{div}^{2\gamma}_{i,j}(A,B,Q) := \left(B_{i,j} - A_{i,j+\frac{1}{2}}\right) Q_{i,j+\frac{1}{2}} + \left(A_{i,j-\frac{1}{2}} - B_{i,j}\right) Q_{i,j-\frac{1}{2}}. \end{cases} \tag{43}$$

Summing (41) and (43), the terms proportional to $A^{\alpha\pm}$ cancel and the full divergence reduces to

$$V^{\pm}_{i,j}\,\mathrm{div}^{\alpha}_{i,j}(B,Q) := B^{\alpha\pm}_{i,j}\big(Q^{\alpha\pm}_{i+\frac{1}{2},j} - Q^{\alpha\pm}_{i-\frac{1}{2},j}\big), \tag{44}$$

which requires no explicit reconstruction of the trimmed control volumes.

It remains to express the face fluxes $Q^{\alpha\pm}$ in terms of the cell unknowns. The first component of the gradient is a staggered average of $\partial_1 c^{\pm}$ over the region between neighboring phase centroids,

$$G^{1\pm}_{i-\frac{1}{2},j} := \frac{1}{W^{1\pm}_{i-\frac{1}{2},j}} \int_{W^{1\pm}_{i-\frac{1}{2},j}} \partial_1 c^{\pm}\, d\mathbf{x}, \qquad W^{1\pm}_{i-\frac{1}{2},j} \neq 0. \tag{45}$$

Applying the Gauss theorem on the staggered region and splitting the boundary into mesh faces and the embedded interface gives

$$\begin{aligned} W^{1\pm}_{i-\frac{1}{2},j}\, G^{1\pm}_{i-\frac{1}{2},j} = {} & B^{1\pm}_{i,j}\, c^{\omega\pm}_{i,j} - B^{1\pm}_{i-1,j}\, c^{\omega\pm}_{i-1,j} \\ & + \big(A^{1\pm}_{i-\frac{1}{2},j} - B^{1\pm}_{i,j}\big)\, c^{\gamma\pm}_{i,j} - \big(A^{1\pm}_{i-\frac{1}{2},j} - B^{1\pm}_{i-1,j}\big)\, c^{\gamma\pm}_{i-1,j}, \end{aligned} \tag{46}$$

where the first line is the bulk contribution and the second line is the interfacial correction. This defines the two gradient operators

$$\begin{cases} \mathrm{grad}^{1\omega}_{i-\frac{1}{2},j}(B,W,c^{\omega\pm}) := \dfrac{B_{i,j}\, c^{\omega\pm}_{i,j} - B_{i-1,j}\, c^{\omega\pm}_{i-1,j}}{W_{i-\frac{1}{2},j}}, \\ \mathrm{grad}^{1\gamma}_{i-\frac{1}{2},j}(A,B,W,c^{\gamma\pm}) := \dfrac{\big(A_{i-\frac{1}{2},j} - B_{i,j}\big)\, c^{\gamma\pm}_{i,j} - \big(A_{i-\frac{1}{2},j} - B_{i-1,j}\big)\, c^{\gamma\pm}_{i-1,j}}{W_{i-\frac{1}{2},j}}. \end{cases} \tag{47}$$

The second component $\mathrm{grad}^{2\omega}$ and $\mathrm{grad}^{2\gamma}$ are defined analogously on the staggered volume $W^{2\pm}_{i,j-\frac{1}{2}}$, replacing $(i-1,j) \to (i,j-1)$ and $B^{1\pm}, A^{1\pm}$ by their y-aligned counterparts.

The constitutive relation $\mathbf{q}^{\pm}_c = -D^{\pm}\nabla c^{\pm}$ is then imposed in discrete form as

$$Q^{1\pm}_{i-\frac{1}{2},j} = -D^{\pm}\left[\mathrm{grad}^{1\omega}_{i-\frac{1}{2},j}\left(B^{1\pm}, W^{1\pm}, c^{\omega\pm}\right) + \mathrm{grad}^{1\gamma}_{i-\frac{1}{2},j}\left(A^{1\pm}, B^{1\pm}, W^{1\pm}, c^{\gamma\pm}\right)\right], \tag{48}$$

and similarly for $Q^{2\pm}_{i,j-\frac{1}{2}}$.

4.1.2 Conservative convection operator

The convective operator is written in conservative flux form. It takes as geometric inputs the phase apertures $A^{\alpha\pm}$ for the Cartesian-face contribution and the pair $(A^{\alpha\pm}, B^{\alpha\pm})$ for the embedded interface contribution. We write

$$\mathrm{conv}^{\pm} = \mathrm{conv}^{\pm}\left(A^{\pm}, B^{\pm}, u^{\omega\pm}, u^{\gamma\pm}, c^{\omega\pm}, c^{\gamma\pm}\right).$$

We first define the aperture-weighted Cartesian face velocities

$$a^{1\omega\pm}_{i+\frac{1}{2},j} = A^{1\pm}_{i+\frac{1}{2},j} u^{1\omega\pm}_{i+\frac{1}{2},j}, \qquad a^{2\omega\pm}_{i,j+\frac{1}{2}} = A^{2\pm}_{i,j+\frac{1}{2}} u^{2\omega\pm}_{i,j+\frac{1}{2}}. \tag{49}$$

The convective fluxes through Cartesian faces are

$$F^{1\omega\pm}_{i+\frac{1}{2},j} = a^{1\omega\pm}_{i+\frac{1}{2},j} \widehat{c}^{\,1\omega\pm}_{i+\frac{1}{2},j}, \qquad F^{2\omega\pm}_{i,j+\frac{1}{2}} = a^{2\omega\pm}_{i,j+\frac{1}{2}} \widehat{c}^{\,2\omega\pm}_{i,j+\frac{1}{2}}. \tag{50}$$

where $\widehat{c}$ denotes, for a centered reconstruction, the arithmetic average of the neighboring cell values,

$$\widehat{c}^{\,1\omega\pm}_{i+\frac{1}{2},j} = \frac{c^{\omega\pm}_{i,j} + c^{\omega\pm}_{i+1,j}}{2}, \qquad \widehat{c}^{\,2\omega\pm}_{i,j+\frac{1}{2}} = \frac{c^{\omega\pm}_{i,j} + c^{\omega\pm}_{i,j+1}}{2}. \tag{51}$$

For an upwind scheme, the upwind state is selected according to the sign of the face mass flux:

$$\begin{aligned} F^{1\omega\pm}_{i+\frac{1}{2},j} &= \left(a^{1\omega\pm}_{i+\frac{1}{2},j}\right)^{+} c^{\omega\pm}_{i,j} + \left(a^{1\omega\pm}_{i+\frac{1}{2},j}\right)^{-} c^{\omega\pm}_{i+1,j}, \\ F^{2\omega\pm}_{i,j+\frac{1}{2}} &= \left(a^{2\omega\pm}_{i,j+\frac{1}{2}}\right)^{+} c^{\omega\pm}_{i,j} + \left(a^{2\omega\pm}_{i,j+\frac{1}{2}}\right)^{-} c^{\omega\pm}_{i,j+1}, \end{aligned} \tag{52}$$

where

$$a^{+} = \max(a, 0), \qquad a^{-} = \min(a, 0).$$

The bulk part of the convective operator is then

$$\begin{cases} V^{\pm}_{i,j} \operatorname{conv}^{1\omega}_{i,j}\left(A^{1\pm}, u^{1\omega\pm}, c^{\omega\pm}\right) := F^{1\omega\pm}_{i+\frac{1}{2},j} - F^{1\omega\pm}_{i-\frac{1}{2},j}, \\ V^{\pm}_{i,j} \operatorname{conv}^{2\omega}_{i,j}\left(A^{2\pm}, u^{2\omega\pm}, c^{\omega\pm}\right) := F^{2\omega\pm}_{i,j+\frac{1}{2}} - F^{2\omega\pm}_{i,j-\frac{1}{2}}. \end{cases} \tag{53}$$

The cut/interface contribution is built with the same geometric weights as the interface part of the divergence operator. We define the oriented cut-face convective coefficients

$$\begin{cases} a^{1\gamma\pm}_{i+\frac{1}{2},j} := \left(B^{1\pm}_{i,j} - A^{1\pm}_{i+\frac{1}{2},j}\right) u^{1\gamma\pm}_{i+\frac{1}{2},j}, \\ a^{1\gamma\pm}_{i-\frac{1}{2},j} := \left(A^{1\pm}_{i-\frac{1}{2},j} - B^{1\pm}_{i,j}\right) u^{1\gamma\pm}_{i-\frac{1}{2},j}, \\ a^{2\gamma\pm}_{i,j+\frac{1}{2}} := \left(B^{2\pm}_{i,j} - A^{2\pm}_{i,j+\frac{1}{2}}\right) u^{2\gamma\pm}_{i,j+\frac{1}{2}}, \\ a^{2\gamma\pm}_{i,j-\frac{1}{2}} := \left(A^{2\pm}_{i,j-\frac{1}{2}} - B^{2\pm}_{i,j}\right) u^{2\gamma\pm}_{i,j-\frac{1}{2}}. \end{cases} \tag{54}$$

The corresponding interface convective fluxes are

$$F^{1\gamma\pm}_{i\pm\frac{1}{2},j} = a^{1\gamma\pm}_{i\pm\frac{1}{2},j} \widehat{c}^{\,1\gamma\pm}_{i\pm\frac{1}{2},j}, \qquad F^{2\gamma\pm}_{i,j\pm\frac{1}{2}} = a^{2\gamma\pm}_{i,j\pm\frac{1}{2}} \widehat{c}^{\,2\gamma\pm}_{i,j\pm\frac{1}{2}}. \tag{55}$$

The reconstruction for the cut/interface contribution must involve both the bulk cell value and the interfacial trace. For a centered reconstruction, we take

$$\widehat{c}^{\,1\gamma\pm}_{i\pm\frac{1}{2},j} = \frac{c^{\omega\pm}_{i,j} + c^{\gamma\pm}_{i,j}}{2}, \qquad \widehat{c}^{\,2\gamma\pm}_{i,j\pm\frac{1}{2}} = \frac{c^{\omega\pm}_{i,j} + c^{\gamma\pm}_{i,j}}{2}. \tag{56}$$

For an upwind reconstruction, the upwind state is selected between the bulk unknown and the interfacial

unknown according to the sign of the oriented coefficient:

$$\widehat{c}_{\star}^{\gamma\pm} = \begin{cases} c_{i,j}^{\omega\pm}, & a_{\star}^{\gamma\pm} \geq 0, \\ c_{i,j}^{\gamma\pm}, & a_{\star}^{\gamma\pm} < 0, \end{cases} \qquad \star \in \left\{ i \pm \frac{1}{2}, j;\, i, j \pm \frac{1}{2} \right\}. \tag{57}$$

The embedded-interface part of the convective operator is

$$\begin{cases} V_{i,j}^{\pm}\, \mathrm{conv}_{i,j}^{1\gamma}\left(A^{1\pm}, B^{1\pm}, u^{1\gamma\pm}, c^{\omega\pm}, c^{\gamma\pm}\right) := F_{i+\frac{1}{2},j}^{1\gamma\pm} + F_{i-\frac{1}{2},j}^{1\gamma\pm}, \\ V_{i,j}^{\pm}\, \mathrm{conv}_{i,j}^{2\gamma}\left(A^{2\pm}, B^{2\pm}, u^{2\gamma\pm}, c^{\omega\pm}, c^{\gamma\pm}\right) := F_{i,j+\frac{1}{2}}^{2\gamma\pm} + F_{i,j-\frac{1}{2}}^{2\gamma\pm}. \end{cases} \tag{58}$$

The signs are contained in the oriented coefficients $a^{\alpha\gamma\pm}$. Therefore the interface contribution is written as a sum, whereas the bulk contribution is written as a difference of Cartesian face fluxes. The total fixed-interface convection operator is

$$\begin{aligned} \mathrm{conv}_{i,j}^{\pm}\left(A^{\pm}, B^{\pm}, u^{\omega\pm}, u^{\gamma\pm}, c^{\omega\pm}, c^{\gamma\pm}\right) := {} & \mathrm{conv}_{i,j}^{1\omega}\left(A^{1\pm}, u^{1\omega\pm}, c^{\omega\pm}\right) + \mathrm{conv}_{i,j}^{2\omega}\left(A^{2\pm}, u^{2\omega\pm}, c^{\omega\pm}\right) \\ & + \mathrm{conv}_{i,j}^{1\gamma}\left(A^{1\pm}, B^{1\pm}, u^{1\gamma\pm}, c^{\omega\pm}, c^{\gamma\pm}\right) + \mathrm{conv}_{i,j}^{2\gamma}\left(A^{2\pm}, B^{2\pm}, u^{2\gamma\pm}, c^{\omega\pm}, c^{\gamma\pm}\right). \end{aligned} \tag{59}$$

4.1.3 Fixed-interface finite-volume balance

Using a θ-scheme in time, the fixed-interface convective–diffusive balance in each active phase cell is

$$\begin{aligned} & \rho^{\pm} V_{i,j}^{\pm} \frac{c_{n+1,i,j}^{\omega\pm} - c_{n,i,j}^{\omega\pm}}{\Delta t_n} + \rho^{\pm} V_{i,j}^{\pm}\, \mathrm{conv}_{i,j}^{\pm}\left(A^{\pm}, B^{\pm}, u_{n+\theta}^{\omega\pm}, u_{n+\theta}^{\gamma\pm}, c_{n+\theta}^{\omega\pm}, c_{n+\theta}^{\gamma\pm}\right) \\ & \quad + \rho^{\pm} \sum_{\alpha=1}^{2} V_{i,j}^{\pm}\, \mathrm{div}_{i,j}^{\alpha\omega}\left(A^{\alpha\pm}, Q_{n+\theta}^{\alpha\pm}\right) + \rho^{\pm} \sum_{\alpha=1}^{2} V_{i,j}^{\pm}\, \mathrm{div}_{i,j}^{\alpha\gamma}\left(A^{\alpha\pm}, B^{\alpha\pm}, Q_{n+\theta}^{\alpha\pm}\right) = V_{i,j}^{\pm} r_{c,n+\theta,i,j}^{\pm}. \end{aligned} \tag{60}$$

The convective term may be treated explicitly, implicitly, or semi-implicitly depending on the chosen time integrator. In the numerical examples below, the centered reconstruction is used for convergence tests.

In mixed cells, the interfacial balance (10) is imposed by equating the total convective–diffusive exchange on the two sides of the interface:

$$\begin{aligned} & \rho^{+} \sum_{\alpha=1}^{2} V_{i,j}^{+}\, \mathrm{div}_{i,j}^{\alpha\gamma}\left(A^{\alpha+}, B^{\alpha+}, Q^{\alpha+}\right) + \rho^{+} \sum_{\alpha=1}^{2} V_{i,j}^{+}\, \mathrm{conv}_{i,j}^{\alpha\gamma}\left(A^{\alpha+}, B^{\alpha+}, u^{\alpha\gamma+}, c^{\omega+}, c^{\gamma+}\right) \\ & \quad - \rho^{-} \sum_{\alpha=1}^{2} V_{i,j}^{-}\, \mathrm{div}_{i,j}^{\alpha\gamma}\left(A^{\alpha-}, B^{\alpha-}, Q^{\alpha-}\right) - \rho^{-} \sum_{\alpha=1}^{2} V_{i,j}^{-}\, \mathrm{conv}_{i,j}^{\alpha\gamma}\left(A^{\alpha-}, B^{\alpha-}, u^{\alpha\gamma-}, c^{\omega-}, c^{\gamma-}\right) = 0. \end{aligned} \tag{61}$$

The second interface equation is the Henry or partition relation

$$c_{i,j}^{\gamma+} - \lambda c_{i,j}^{\gamma-} = g_{\Gamma,i,j}. \tag{62}$$

4.1.4 Kapitza thermal resistance at the interface

For thermal transport with Kapitza resistance, the discrete balance replaces the Henry equation (9) with a Robin condition on the interface. In mixed cells, the thermal interface balance is then:

$$k^+ \sum_{\alpha=1}^{2} V_{i,j}^{+} \operatorname{div}_{i,j}^{\alpha\gamma} \left(A^{\alpha+}, B^{\alpha+}, Q^{\alpha+}\right) - k^- \sum_{\alpha=1}^{2} V_{i,j}^{-} \operatorname{div}_{i,j}^{\alpha\gamma} \left(A^{\alpha-}, B^{\alpha-}, Q^{\alpha-}\right) = -\frac{T_{i,j}^{\gamma+} - T_{i,j}^{\gamma-}}{R_{K,i,j}} |\Gamma_{i,j}|, \quad (63)$$

where $R_{K,i,j}$ is the Kapitza resistance and $|\Gamma_{i,j}|$ is the area of the interface fragment. This equation couples the interfacial heat flux to the temperature jump through the Kapitza resistance. The right-hand side arises from integrating the temperature jump $-[\![T]\!]/R_K$ over the interface area. In the limit $R_K \to 0$, the interface approaches perfect thermal contact and the temperature jump vanishes. In the opposite limit $R_K \to \infty$, the interfacial heat flux tends to zero and the temperature jump is not constrained by the resistance law.

4.2 Space–time operators for moving interfaces

We now extend our discrete operators over the space–time interval $[t_n, t_{n+1}]$. Reynolds' theorem applied to the moving phase-restricted cell gives the following identity :

$$\frac{d}{dt} \int_{\Omega_{i,j}^{\pm}(t)} \rho^{\pm} c^{\pm} \, dV = \int_{\Omega_{i,j}^{\pm}(t)} \partial_t (\rho^{\pm} c^{\pm}) \, dV + \int_{\Gamma_{i,j}(t)} \rho^{\pm} c^{\pm} \mathbf{w} \cdot \mathbf{n}^{\pm} \, dS. \quad (64)$$

Combining (64) with the conservative bulk equation (3) gives the following space–time cell balance

$$\begin{aligned} \rho^{\pm} \left(V_{n+1,i,j}^{\pm} c_{n+1,i,j}^{\omega\pm} - V_{n,i,j}^{\pm} c_{n,i,j}^{\omega\pm} \right) & \\ + \int_{t_n}^{t_{n+1}} \int_{\partial\Omega_{i,j}^{\pm}(t) \setminus \Gamma_{i,j}(t)} & \left(\rho^{\pm} c^{\pm} \mathbf{u}^{\pm} + \mathbf{j}_c^{\pm}\right) \cdot \mathbf{n}^{\pm} \, dS \, dt \\ + \int_{t_n}^{t_{n+1}} \int_{\Gamma_{i,j}(t)} & \left[\rho^{\pm} c^{\pm} \left(\mathbf{u}^{\pm} - \mathbf{w}\right) + \mathbf{j}_c^{\pm}\right] \cdot \mathbf{n}^{\pm} \, dS \, dt = \mathcal{V}_{n+\frac{1}{2},i,j}^{\pm} \mathcal{R}_{c,n+\frac{1}{2},i,j}^{\pm}. \end{aligned} \quad (65)$$

where the space–time source average is

$$\mathcal{R}_{c,n+\frac{1}{2},i,j}^{\pm} = \frac{\displaystyle\int_{t_n}^{t_{n+1}} \int_{\Omega_{i,j}^{\pm}(t)} r_c^{\pm}(t, \mathbf{x}) \, dV \, dt}{\mathcal{V}_{n+\frac{1}{2},i,j}^{\pm}}. \quad (66)$$

with

$$\mathcal{V}_{n+\frac{1}{2},i,j}^{\pm} = \int_{t_n}^{t_{n+1}} \int_{\Omega_{i,j}^{\pm}(t)} dV \, dt.$$

Thus the convective flux appears through the relative velocity $\mathbf{u}^{\pm} - \mathbf{w}$. This is the continuous formulation that the discrete space–time operator must reproduce.

Space–time diffusive fluxes are obtained from the fixed-interface gradient operator by replacing (A, B, W), with $(\mathcal{A}, \mathcal{B}, \mathcal{W})$ and by using the slab-averaged bulk and interface states, as illustrated in Figure 2. The slab-averaged bulk state is defined by the usual θ interpolation in persistent cells,

$$\overline{c}_{n+\theta,i,j}^{\omega\pm} = (1-\theta) c_{n,i,j}^{\omega\pm} + \theta c_{n+1,i,j}^{\omega\pm}, \qquad V_{n,i,j}^{\pm} V_{n+1,i,j}^{\pm} > 0. \quad (67)$$

For fresh or dead phase cells, where one of the end-time volumes vanishes, the same conservative balance is retained and the slab state is set to the new end-time value. This is the moving-interface diffusive

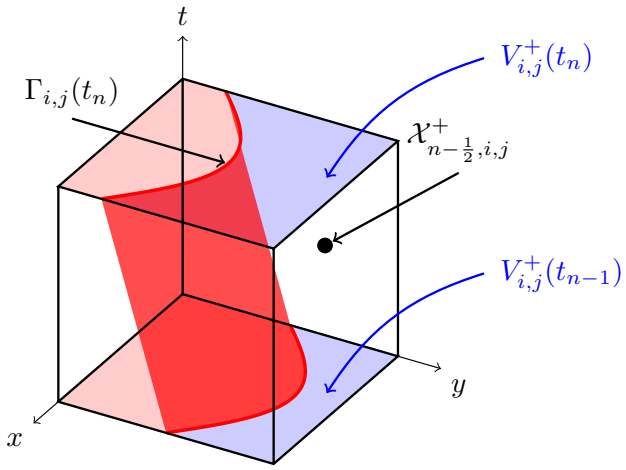

Figure 2: Space-time control volume over $]t_n, t_{n+1}[$ illustrating the phase-restricted sub-volumes $V^+_{i,j}(t_n)$ and $V^+_{i,j}(t_{n+1})$ and the swept interface within the time interval.

space–time closure, as explained in [29], and prevents creation or deletion of scalar mass outside the flux balance. The space-time diffusive flux is written in the first direction as :

$$Q^{1\pm}_{n+\frac{1}{2},i-\frac{1}{2},j} = -D^{\pm}\left[\mathrm{grad}^{1\omega}_{i-\frac{1}{2},j}\left(\mathcal{B}^{1\pm},\mathcal{W}^{1\pm},\widetilde{c}^{\omega\pm}_{n+\theta}\right) + \mathrm{grad}^{1\gamma}_{i-\frac{1}{2},j}\left(\mathcal{A}^{1\pm},\mathcal{B}^{1\pm},\mathcal{W}^{1\pm},c^{\gamma\pm}_{n+\theta}\right)\right], \tag{68}$$

and analogously in the second coordinate direction.

The conservative space–time convection operator is assembled with the same methodology. The bulk part uses the time-integrated aperture velocity and the interfacial part uses the oriented cut-cell coefficients associated with $\mathcal{B}-\mathcal{A}$, similarly as in (54). This defines the extended space-time convection operator :

$$\mathrm{conv}^{\pm}_{i,j}\left(\mathcal{A}^{\pm},\mathcal{B}^{\pm},\widetilde{u}^{\omega\pm},\widetilde{u}^{\gamma\pm},\widetilde{c}^{\omega\pm}_{n+\theta},c^{\gamma\pm}_{n+\theta}\right), \tag{69}$$

with centered or upwind reconstructions identical to (51)–(57).

The geometric conservation law (GCL) follows from (64) with a constant concentration and zero physical flux:

$$V^{\pm}_{n+1,i,j} - V^{\pm}_{n,i,j} - \int_{t_n}^{t_{n+1}}\int_{\Gamma_{i,j}(t)} \mathbf{w}\cdot\mathbf{n}^{\pm}\,dS\,dt = 0. \tag{70}$$

Using this identity, the interfacial flux contribution may be written directly as a volume variation. This is the cut-cell version of the discrete geometric conservation law used in moving-mesh finite-volume schemes [5].The discrete bulk balance becomes

$$\begin{aligned}
&\rho^{\pm}\left(V^{\pm}_{n+1,i,j}c^{\omega\pm}_{n+1,i,j} - V^{\pm}_{n,i,j}c^{\omega\pm}_{n,i,j}\right)\\
&\qquad + \rho^{\pm}\mathcal{V}^{\pm}_{n+\frac{1}{2},i,j}\,\mathrm{conv}^{\pm}_{i,j}\left(\mathcal{A}^{\pm},\mathcal{B}^{\pm},\widetilde{u}^{\omega\pm},\widetilde{u}^{\gamma\pm},\widetilde{c}^{\omega\pm}_{n+\theta},c^{\gamma\pm}_{n+\theta}\right)\\
&+ \rho^{\pm}\sum_{\alpha=1}^{2}\mathcal{V}^{\pm}_{n+\frac{1}{2},i,j}\,\mathrm{div}^{\alpha\omega}_{i,j}\left(\mathcal{A}^{\alpha\pm},Q^{\alpha\pm}_{n+\frac{1}{2}}\right) + \rho^{\pm}\sum_{\alpha=1}^{2}\mathcal{V}^{\pm}_{n+\frac{1}{2},i,j}\,\mathrm{div}^{\alpha\gamma}_{i,j}\left(\mathcal{A}^{\alpha\pm},\mathcal{B}^{\alpha\pm},Q^{\alpha\pm}_{n+\frac{1}{2}}\right)\\
&\qquad - \rho^{\pm}c^{\gamma\pm}_{n+\frac{1}{2},i,j}\left(V^{\pm}_{n+1,i,j} - V^{\pm}_{n,i,j}\right) = \mathcal{V}^{\pm}_{n+\frac{1}{2},i,j}\mathcal{R}^{\pm}_{c,n+\frac{1}{2},i,j}.
\end{aligned} \tag{71}$$

In mixed cells, the discrete interface condition is the space–time counterpart of (7). Written with the

cut-cell operators, it reads

$$\rho^{+}\mathcal{V}^{+}_{n+\frac{1}{2},i,j}\sum_{\alpha=1}^{2}\mathrm{conv}^{\alpha\gamma}_{i,j}\left(\mathcal{A}^{\alpha+},\mathcal{B}^{\alpha+},\widetilde{u}^{\alpha\gamma+},\widetilde{c}^{\omega+}_{n+\theta},c^{\gamma+}_{n+\theta}\right)+\rho^{+}\mathcal{V}^{+}_{n+\frac{1}{2},i,j}\sum_{\alpha=1}^{2}\mathrm{div}^{\alpha\gamma}_{i,j}\left(\mathcal{A}^{\alpha+},\mathcal{B}^{\alpha+},\mathcal{Q}^{\alpha+}\right)$$
$$-\rho^{-}\mathcal{V}^{-}_{n+\frac{1}{2},i,j}\sum_{\alpha=1}^{2}\mathrm{conv}^{\alpha\gamma}_{i,j}\left(\mathcal{A}^{\alpha-},\mathcal{B}^{\alpha-},\widetilde{u}^{\alpha\gamma-},\widetilde{c}^{\omega-}_{n+\theta},c^{\gamma-}_{n+\theta}\right)-\rho^{-}\mathcal{V}^{-}_{n+\frac{1}{2},i,j}\sum_{\alpha=1}^{2}\mathrm{div}^{\alpha\gamma}_{i,j}\left(\mathcal{A}^{\alpha-},\mathcal{B}^{\alpha-},\mathcal{Q}^{\alpha-}\right)$$
$$-\left(\rho^{+}c^{\gamma+}_{n+\theta,i,j}-\rho^{-}c^{\gamma-}_{n+\theta,i,j}\right)\left(V^{-}_{n+1,i,j}-V^{-}_{n,i,j}\right)=0. \quad (72)$$

If the interface is transported by the flow, $\mathbf{u}^{\pm}\cdot\mathbf{n}=\mathbf{w}\cdot\mathbf{n}$, the interface contributions cancel out. The remaining interface condition is then the diffusive Henry balance, translated with the interface.

Finally, the second equation in each mixed cell is the space–time partition law

$$c^{\gamma+}_{n+\theta,i,j}-\lambda c^{\gamma-}_{n+\theta,i,j}=\widetilde{g}_{\Gamma,n+\theta,i,j}. \quad (73)$$

with

$$\widetilde{g}_{\Gamma,n+\theta,i,j}=\frac{\displaystyle\int_{t_n}^{t_{n+1}}\int_{\Gamma_{i,j}(t)}g_{\Gamma}(t,\mathbf{x})\,dS\,dt}{\displaystyle\int_{t_n}^{t_{n+1}}\int_{\Gamma_{i,j}(t)}dS\,dt}. \quad (74)$$

5. Numerical results

The numerical section reports results from different benchmarks. We report grid convergence, interface-condition residuals, and global conservation errors on three benchmarks designed to isolate the diffusive Henry coupling (Section 5.1), the conservative space–time convection (Section 5.2), and the Kapitza thermal contact condition (Section 5.3), respectively.

5.1 Static Henry jump on a circular water/air interface

The first test is a two-dimensional unsteady concentration problem with a fixed circular interface. The computational domain is the square box $\Omega=[0,4]^2$, and the disk of radius $R=1$ is centered in Ω, so that the outer boundary $\partial\Omega$ remains far from the interface. Homogeneous Neumann conditions $\nabla c^{\pm}\cdot\mathbf{n}_{\partial\Omega}=0$ are imposed on $\partial\Omega$. The computation is advanced to $t_{\mathrm{end}}=3.2s$. We use a water/air partition case with $\frac{D_g}{D_l}=100,\lambda=30$. The interface is static and there is no bulk flow, $\mathbf{w}=\mathbf{0},\mathbf{u}^{\pm}=\mathbf{0}$, , so the governing problem is unsteady diffusion in the two phases,

$$\frac{\partial c^{\pm}}{\partial t}=\nabla\cdot\left(D^{\pm}\nabla c^{\pm}\right),\qquad \mathbf{x}\in\Omega^{\pm}. \quad (75)$$

The interface conditions are

$$[\![\mathbf{j}_c\cdot\mathbf{n}]\!]=0,\qquad c^{+}-\lambda c^{-}=g_{\Gamma}. \quad (76)$$

The bulk diffusion problem (75) with interface conditions (76) is challenging: the Henry jump and diffusivity ratio are both large. The test verifies that a discontinuous concentration is represented without smearing and that the interfacial fluxes remain conservative in time. The primary scalar diagnostic is the mean normal flux through the interface, which we measure as in,

$$\overline{q}_{n,g}=\frac{1}{|\Gamma|}\int_{\Gamma}\mathbf{j}^{+}_{c}\cdot\mathbf{n}\,dS,\qquad \overline{q}_{n,l}=\frac{1}{|\Gamma|}\int_{\Gamma}\mathbf{j}^{-}_{c}\cdot\mathbf{n}\,dS, \quad (77)$$

with the corresponding bulk concentrations c_g and c_l. The analytical reference solution for this configuration can be found in [28].

Errors are reported as relative L^2 norms. For a discrete field c with analytical reference c^{ana} sampled on the same unknowns, indexed by k, we define

$$\frac{\|c - c^{\mathrm{ana}}\|}{\|c^{\mathrm{ana}}\|} = \left(\frac{\sum_k \left(c_k - c_k^{\mathrm{ana}} \right)^2}{\sum_k \left(c_k^{\mathrm{ana}} \right)^2} \right)^{1/2} . \tag{78}$$

Here N_x is the number of cells in each Cartesian direction over the computational box of side L, so $N_{\mathrm{diam}} = 2R\,N_x/L$. The time step is refined together with the mesh to keep the diffusive Fourier number $\mathrm{Fo} = D^{\pm}\Delta t/h^2$ – the ratio of the time-step size Δt to the diffusive time scale $h^2/D^{\pm}$ – bounded as $h \to 0$. Table 1 compares the bulk concentration relative L^2 error with a one-fluid method, in which a single mixture concentration is advanced on the Cartesian mesh and the Henry jump is recovered only through a post-processed reconstruction of the traces, following the one-fluid approach used in Basilisk [32]. The present method gives the same coarse result at one cell per diameter, but rapidly becomes more accurate as the interface is resolved, since the jump is represented exactly by construction rather than reconstructed a posteriori. The present method converges faster, approaching second order rates.

N_{diam}	Two-fluid $\|c - c^{\mathrm{ana}}\|/\|c^{\mathrm{ana}}\|$	One-fluid $\|c - c^{\mathrm{ana}}\|/\|c^{\mathrm{ana}}\|$	Gain
1	3.25×10^{-1}	3.25×10^{-1}	×1.0
2	7.82×10^{-3}	1.85×10^{-2}	×2.4
4	1.54×10^{-3}	9.32×10^{-3}	×6.1
8	3.24×10^{-4}	5.45×10^{-3}	×16.8
16	5.25×10^{-5}	2.75×10^{-3}	×52.4
32	6.46×10^{-6}	1.42×10^{-3}	×220
128	1.94×10^{-7}	3.32×10^{-4}	×1711

Table 1: Static unsteady Henry disk problem: relative L^2 error (78) on the solution errors, obtained with the present two-fluid cut-cell method and with a one-fluid method. The gain is the ratio between the one-fluid and two-fluid relative errors. The gain exceeds 10^3 on the finest mesh.

Table 2 reports the convergence of the interface transfer quantities at $t_{\mathrm{end}} = 3.2$. The coarsest level $N_x = 16$ remains pre-asymptotic, but from $N_x = 32$ onward both the mean interface flux and the interfacial concentration converge at approximately second order.

N_x	h	Δt	$\overline{q}_{n,g}$	$\max e_q$	p_q	$\max e_{c_\Gamma}$	p_c
16	0.625	1.9531×10^{-1}	0.373194	1.50×10^{-1}	–	2.46×10^{-1}	–
32	0.3125	4.8828×10^{-2}	0.280463	5.75×10^{-2}	1.38	6.15×10^{-2}	2.00
64	0.15625	1.2207×10^{-2}	0.227836	4.88×10^{-3}	3.56	2.14×10^{-2}	1.52
128	0.078125	3.0518×10^{-3}	0.224071	1.12×10^{-3}	2.13	5.43×10^{-3}	1.98
256	0.0390625	7.6294×10^{-4}	0.223222	2.67×10^{-4}	2.06	1.37×10^{-3}	1.99

Table 2: Static unsteady Henry disk: convergence of the interfacial transfer quantities. The reported flux error is $\max(|\overline{q}_{n,g} - \overline{q}_{n,g}^{\mathrm{ana}}|, |\overline{q}_{n,l} - \overline{q}_{n,l}^{\mathrm{ana}}|)$ and the concentration error is the corresponding maximum over the two interface traces.

5.2 Co-moving convective Henry benchmark: rigid rotation

The second test reuses the circular interface and the Henry law, but the disk and the surrounding flow undergo a rigid-body rotation about the center $\mathbf{x}_c$ with angular velocity ϖ. The Eulerian velocity field is

then

$$\mathbf{u}^{\pm}(\mathbf{x},t) = \varpi\,\mathbf{e}_z \times (\mathbf{x}-\mathbf{x}_c), \qquad \mathbf{w}(\mathbf{x},t) = \varpi\,\mathbf{e}_z \times (\mathbf{x}-\mathbf{x}_c) \quad \text{on } \Gamma(t), \tag{79}$$

so that, on the interface,

$$\big(\mathbf{u}^{\pm} - \mathbf{w}\big)\cdot\mathbf{n} = 0 \qquad \text{on } \Gamma(t). \tag{80}$$

The flow is solenoidal, $\nabla\cdot\mathbf{u}^{\pm} = 0$, and the disk is transported rigidly: the solution in the co-rotating frame must reproduce the static Henry solution,

$$c^{\pm}(\mathbf{x},t) = c_0^{\pm}\big(\mathsf{R}_{-\varpi t}(\mathbf{x}-\mathbf{x}_c) + \mathbf{x}_c\big), \tag{81}$$

where R_ϕ denotes the rotation matrix of angle ϕ. The kinematics (79) give the zero relative normal velocity (80), so that the co-rotating solution (81) reproduces the static Henry case. This benchmark simultaneously tests the conservative convection operator, the space–time moments, the GCL, and the treatment of fresh/dead cells.

We use the same water/air Henry contrast as the static disk, $\lambda = 30$ and $D_g/D_l = 100$, with $\varpi = 0.1$ rad/s and $t_{\text{end}} = 3.2s$, so that the disk undergoes a non-trivial but moderate rotation. Table 3 reports the L^2 error of the bulk concentration in each phase and the combined error, against the rotated reference solution. Refined meshes recover between first- and second-order convergence on the combined error, with the gas-side error converging close to second order. At the finest mesh, the numerical residual of the Henry jump relation is 7.1×10^{-15}, and the transport flux-row residual is 2.6×10^{-17}. The latter two quantities confirm that the conservative convection operator and the sweeping contribution cancel to machine precision.

N	h	comb. err	p	gas err	p_g	liq err	p_l
8	1.2500	1.153×10^{-1}	–	1.907×10^{-1}	–	1.120×10^{-1}	–
12	8.333×10^{-1}	3.954×10^{-2}	2.64	6.883×10^{-2}	2.51	3.822×10^{-2}	2.65
16	6.250×10^{-1}	3.767×10^{-2}	0.17	3.195×10^{-2}	2.67	3.784×10^{-2}	0.03
24	4.167×10^{-1}	1.764×10^{-2}	1.87	4.071×10^{-3}	5.08	1.791×10^{-2}	1.85
32	3.125×10^{-1}	1.116×10^{-2}	1.59	2.115×10^{-3}	2.28	1.133×10^{-2}	1.59
48	2.083×10^{-1}	5.813×10^{-3}	1.61	7.058×10^{-4}	2.71	5.905×10^{-3}	1.61
64	1.563×10^{-1}	3.652×10^{-3}	1.62	3.899×10^{-4}	2.06	3.710×10^{-3}	1.62

Table 3: Rotating two-phase Henry benchmark with analytical reference ($\lambda = 30$, $D_g/D_l = 100$, $\varpi = 0.1$, $t_{\text{end}} = 3.2$). Combined L^2 error on the bulk concentration and per-phase errors, with observed convergence orders p between consecutive mesh levels. The gas-side error converges close to second order; the liquid-side error dominates the combined norm because of the large D_g/D_l ratio and converges between first and second order over the resolved range.

5.3 Kapitza thermal resistance: spherical benchmark

Following the benchmark of [31], the third test considers the Kapitza thermal resistance framework on a three-dimensional spherical shell geometry in a co-moving frame. Two concentric spheres with radii $r_1 = 1.0$ m and $r_2 = 3.0$ m define the interface and outer boundaries. The thermal conductivities are $k_1 = 0.01$ W/(m K) (inner sphere) and $k_2 = 1.0$ W/(m K) (outer region). The Kapitza resistance is $R_K = 4.0$ K m^2/W. Boundary conditions impose a radial temperature gradient $e_0 = 1.0$ K/m. The Robin condition reads

$$T_\Gamma^{(2)} - T_\Gamma^{(1)} - R_K\left[k_2\nabla T^{(2)}\cdot\mathbf{n} - k_1\nabla T^{(1)}\cdot\mathbf{n}\right] = 0. \tag{82}$$

The interface is translated with a co-moving velocity, so $(\mathbf{u}^{\pm}-\mathbf{w})\cdot\mathbf{n} = 0$, and the solution in the moving frame should reproduce the static Kapitza solution. This test simultaneously validates the space–time operators, the geometric conservation law, and the Kapitza condition under interface motion.

Figure 3 shows the three-dimensional temperature field. Table 4 reports the L^2 error of the bulk

temperature and of the interface-jump error across mesh refinement. The algebraic residuals of the flux and Robin equations are enforced by the solver and remain at machine precision. In this benchmark the inner sphere corresponds to the reference − phase (label (1)) and the outer region to the + phase (label (2)), so (82) is the spherical instance of the discrete Kapitza balance (63).

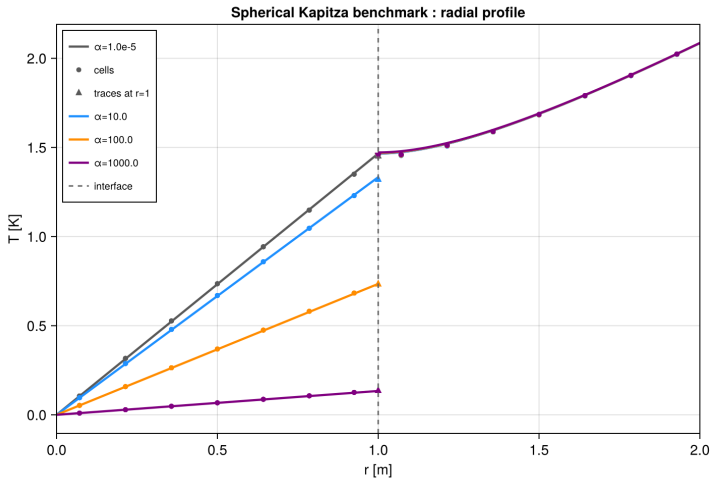

Figure 3: Three-dimensional spherical Kapitza resistance benchmark in co-moving frame: temperature field in the inner and outer regions with the interface at $r = 1.0$ m. The thermal conductivity ratio and Kapitza resistance create a temperature jump across the interface.

R_K	N	h	L^2 bulk	p_{bulk}
10^{-5}	16	0.2500	2.941×10^{-2}	–
10^{-5}	20	0.2000	2.351×10^{-2}	1.00
10^{-5}	28	0.1429	1.032×10^{-2}	2.45
10^{-5}	40	0.1000	5.316×10^{-3}	1.86
10^{-5}	56	0.07143	2.767×10^{-3}	1.94
10^{+1}	16	0.2500	2.727×10^{-2}	–
10^{+1}	20	0.2000	2.215×10^{-2}	0.93
10^{+1}	28	0.1429	9.556×10^{-3}	2.50
10^{+1}	40	0.1000	4.835×10^{-3}	1.91
10^{+1}	56	0.07143	2.612×10^{-3}	1.83
10^{+2}	16	0.2500	2.156×10^{-2}	–
10^{+2}	20	0.2000	1.861×10^{-2}	0.66
10^{+2}	28	0.1429	7.579×10^{-3}	2.67
10^{+2}	40	0.1000	3.876×10^{-3}	1.88
10^{+2}	56	0.07143	1.998×10^{-3}	1.97
10^{+3}	16	0.2500	1.889×10^{-2}	–
10^{+3}	20	0.2000	1.665×10^{-2}	0.56
10^{+3}	28	0.1429	6.696×10^{-3}	2.71
10^{+3}	40	0.1000	3.340×10^{-3}	1.95
10^{+3}	56	0.07143	1.768×10^{-3}	1.89

Table 4: Kapitza spherical benchmark: L^2 errors on the bulk temperature for four values of the Kapitza resistance R_K and various mesh refinements. The bulk error converges, with effective orders rising from sub-first on the coarsest meshes to nearly second order on the finest. The algebraic flux and Robin residuals enforced by the solver remain below 10^{-10} in all runs and are not reported.

6. Conclusion and Future Work

We developed a two-fluid space–time cut-cell finite-volume method for convective–diffusive transport of heat and mass across sharp, moving interfaces. The approach maintains separate phase-specific unknowns and interfacial traces through a moment-based cut-cell discretization, allowing direct enforcement of interface conditions without resorting to one-fluid averaging or reconstruction within mixed cells. A key innovation is the conservative convection operator, which properly accounts for transport relative to the moving interface by coupling the physical convective flux with the geometric sweeping flux through the relative velocity $\mathbf{u} - \mathbf{w}$. The space–time integral balance is constructed such that it intrinsically satisfies the discrete geometric conservation law, preventing spurious sources and sinks of scalar mass or energy due to grid motion.

The method provides a unified framework that accommodates Henry partition laws and Kapitza thermal contact resistance through alternative interface coupling equations, all without modifying the bulk operators or geometry. This flexibility is demonstrated through comprehensive numerical validation: Henry mass transfer on fixed and moving circular interfaces, and Kapitza thermal resistance on concentric spheres in a co-moving frame, showing robust convergence and flux conservation across multiple parameter regimes.

The immediate extension is to coupled heat–mass phase change, where the interface velocity becomes an unknown to be determined jointly by the thermal and solute Stefan balances. This couples the interface motion to the interfacial temperature and concentration through the latent heat and partition law, requiring solution of a nonlinear system at each time step. The present framework is already well-suited for this extension: the space–time operators naturally accommodate phase-change terms, and the interface unknowns provide the degrees of freedom needed to enforce both energy and mass balances simultaneously. The implementation requires only modification of the interface-coupling equations to include the phase-change jump conditions (14) and (6), leaving the moment-based geometry and bulk discretization unchanged. Preliminary work on this extension is currently underway using the existing solvers.

Beyond phase change, several research directions follow naturally from the present framework. The inclusion of surface tension and curvature-dependent interface conditions is relevant for droplet dynamics and interfacial instabilities. Our moment-based geometry already computes interface curvature, and the main task would be consistent discretization of the surface-tension stress at the interface. Reactive transport, where fast chemical reactions occur at the interface or in boundary layers, is another avenue: the two-fluid formulation naturally separates phase-side reaction rates, and the interface unknowns can accommodate reaction-driven partition laws and kinetic limitations. Application to three-dimensional complex geometries, including pore-scale flows in heterogeneous media, CO_2 dissolution and storage, and liquid–vapor equilibrium in composite materials, is enabled by the moment-based approach, which avoids explicit cut-cell construction and suits time-dependent volume-of-fluid representations of complex interfaces on Cartesian grids. Finally, multiscale coupling to derive upscaling laws for Kapitza resistance and Henry constants from molecular or fine-scale simulations would inform macroscale phase-field or sharp-interface models.

References

[1] R. B. Bird, W. E. Stewart, and E. N. Lightfoot. *Transport Phenomena*. Wiley, New York, revised ed. edition, 2007.

[2] E. L. Cussler. *Diffusion: Mass Transfer in Fluid Systems*. Cambridge University Press, 3 edition, 2009.

[3] R. Sander. Compilation of Henry's law constants (version 5.0.0) for water as solvent. *Atmospheric Chemistry and Physics*, 23(19):10901–12440, 2023.

[4] C. W. Hirt, A. A. Amsden, and J. L. Cook. An arbitrary Lagrangian-Eulerian computing method

for all flow speeds. *Journal of Computational Physics*, 14(3):227–253, 1974.

[5] C. Farhat, P. Geuzaine, and C. Grandmont. The discrete geometric conservation law and the nonlinear stability of ALE schemes for the solution of flow problems on moving grids. *Journal of Computational Physics*, 174(2):669–694, 2001.

[6] C. W. Hirt and B. D. Nichols. Volume of fluid (VOF) method for the dynamics of free boundaries. *Journal of Computational Physics*, 39(1):201–225, 1981.

[7] S. Osher and J. A. Sethian. Fronts propagating with curvature-dependent speed: Algorithms based on Hamilton-Jacobi formulations. *Journal of Computational Physics*, 79(1):12–49, 1988.

[8] S. Popinet. An accurate adaptive solver for surface-tension-driven interfacial flows. *Journal of Computational Physics*, 228(16):5838–5866, 2009.

[9] Nour Djaballah, Benoît Trouette, Eric Chénier, Can Selçuk, and Stéphane Vincent. A new two-phase numerical model for species transfer in bubble flows: Comparison with the one-fluid method. SSRN preprint, 2026. Available at SSRN: `https://ssrn.com/abstract=6560006`.

[10] Y. Haroun, D. Legendre, and L. Raynal. Volume of fluid method for interfacial reactive mass transfer: Application to stable liquid film. *Chemical Engineering Science*, 65(10):2896–2909, 2010.

[11] D. Bothe and S. Fleckenstein. A volume-of-fluid-based method for mass transfer processes at fluid particles. *Chemical Engineering Science*, 101:283–302, 2013.

[12] J. Maes and C. Soulaine. A unified single-field volume-of-fluid-based formulation for multi-component interfacial transfer with local volume changes. *Journal of Computational Physics*, 402:109024, 2020.

[13] C. P. Zanutto, E. E. Paladino, F. Evrard, B. van Wachem, and F. Denner. Modeling of interfacial mass transfer based on a single-field formulation and an algebraic VOF method considering non-isothermal systems and large volume changes. *Chemical Engineering Science*, 247:116855, 2022.

[14] Q. Zhang, Y. Yang, L. Zhang, H. Sun, J. Zhong, K. Zhang, and J. Yao. Improved single-field VOF method for interfacial mass transfer modeling: Application to CO2-EOR and carbon sequestration in hydrocarbon reservoirs. *International Journal of Heat and Mass Transfer*, 255:127807, 2026.

[15] L. Yang, L. Fries, Y. M. Harshe, E. A. J. F. Peters, J. A. M. Kuipers, and M. W. Baltussen. Direct numerical simulation of mass transfer and mixing in complex two-phase systems using a coupled volume of fluid and immersed boundary method. *Chemical Engineering Science: X*, 5:100059, 2020.

[16] C. S. Peskin. Flow patterns around heart valves: A numerical method. *Journal of Computational Physics*, 10(2):252–271, 1972.

[17] R. Mittal and G. Iaccarino. Immersed boundary methods. *Annual Review of Fluid Mechanics*, 37(1):239–261, 2005.

[18] F. Gibou, R. P. Fedkiw, L.-T. Cheng, and M. Kang. A second-order-accurate symmetric discretization of the Poisson equation on irregular domains. *Journal of Computational Physics*, 176(1):205–227, 2002.

[19] H. Johansen and P. Colella. A Cartesian grid embedded boundary method for Poisson's equation on irregular domains. *Journal of Computational Physics*, 147(1):60–85, 1998.

[20] P. McCorquodale, P. Colella, and H. Johansen. A Cartesian grid embedded boundary method for the heat equation on irregular domains. *Journal of Computational Physics*, 173(2):620–635, 2001.

[21] P. Schwartz, M. Barad, P. Colella, and T. Ligocki. A Cartesian grid embedded boundary method for the heat equation and Poisson's equation in three dimensions. *Journal of Computational Physics*, 211(2):531–550, 2006.

[22] Alejandro Quirós Rodríguez, Tomas Fullana, Vincent Le Chenadec, and Taraneh Sayadi. A levelset-based cut-cell method for interfacial flows: part 1—Navier–Stokes equations and Rayleigh–Bénard instability with melting boundary. *Acta Mechanica*, 236(9):5763–5786, September 2025.

[23] D. Calhoun and R. J. LeVeque. A Cartesian grid finite-volume method for the advection-diffusion equation in irregular geometries. *Journal of Computational Physics*, 157(1):143–180, 2000.

[24] B. Mirtich. Fast and accurate computation of polyhedral mass properties. *Journal of Graphics Tools*, 1(2):31–50, 1996.

[25] R. I. Saye. High-order quadrature methods for implicitly defined surfaces and volumes in hyper-rectangles. *SIAM Journal on Scientific Computing*, 37(2):A993–A1019, 2015.

[26] A. Chierici, L. Chirco, V. Le Chenadec, R. Scardovelli, P. Yecko, and S. Zaleski. An optimized VOFI library to initialize the volume fraction field. *Computer Physics Communications*, 281:108506, 2022.

[27] D. Dupuy, A. Toutant, A. du Cluzeau, and G. Bois. Time integration of cut-cell surfaces for geometric conservation, applied to scalar transport with moving interfaces. *Computers and Fluids*, 295:106627, 2025.

[28] Nour El Houda Djaballah. *Méthodes à deux champs pour la résolution numérique sur maillages structurés du transfert de masse entre fluides immiscibles : validation et comparaison au modèle à 1-fluide*. Phd thesis, Université Gustave Eiffel, 2026. HAL: tel-05593604; TH2026UEFL2017.

[29] Louis Libat, Can Selçuk, Eric Chénier, and Vincent Le Chenadec. A Space-Time Cartesian Cut-Cell Method for Two-Phase Diffusion Problems using a Two-Fluid Approach. January 2026.

[30] G. L. Pollack. Kapitza Resistance. *Reviews of Modern Physics*, 41(1):48–81, January 1969.

[31] J. Yvonnet, Q. C. He, Q. Z. Zhu, and J. F. Shao. A general and efficient computational procedure for modelling the Kapitza thermal resistance based on XFEM. *Computational Materials Science*, 50(5):1223–1230, 2011.

[32] S. Popinet and others. Basilisk. `http://basilisk.fr`, 2018.